nature chemical biology

ARTICLE

PUBLISHED ONLINE: 6 JULY 2015 | DOI: 10.1038/NCHEMBIO.1857

Strand separation establishes a sustained lock at the Tus–*Ter* replication fork barrier

Bojk A Berghuis[1], David Dulin[1,3], Zhi-Qiang Xu[2], Theo van Laar[1], Bronwen Cross[1], Richard Janissen[1], Slobodan Jergic[2], Nicholas E Dixon[2], Martin Depken[1] & Nynke H Dekker[1]*

The bidirectional replication of a circular chromosome by many bacteria necessitates proper termination to avoid the head-on collision of the opposing replisomes. In *Escherichia coli*, replisome progression beyond the termination site is prevented by Tus proteins bound to asymmetric *Ter* sites. Structural evidence indicates that strand separation on the blocking (nonpermissive) side of Tus–*Ter* triggers roadblock formation, but biochemical evidence also suggests roles for protein-protein interactions. Here DNA unzipping experiments demonstrate that nonpermissively oriented Tus–*Ter* forms a tight lock in the absence of replicative proteins, whereas permissively oriented Tus–*Ter* allows nearly unhindered strand separation. Quantifying the lock strength reveals the existence of several intermediate lock states that are impacted by mutations in the lock domain but not by mutations in the DNA-binding domain. Lock formation is highly specific and exceeds reported *in vivo* efficiencies. We postulate that protein-protein interactions may actually hinder, rather than promote, proper lock formation.

DNA replication in *E. coli* initiates bidirectionally at *oriC,* creating two replication forks that proceed around the circular 4.6-Mbp chromosome in opposite directions. The forks progress at an average speed of 1 kbp/s until they meet again at the terminus region. As the replication forks approach the terminus, each encounters five 23-bp *Ter* DNA sites (out of a total of ten, denoted *TerA–J*; **Fig. 1a**) bound in a specific orientation by a 36-kDa DNA-binding protein called Tus[1–4] and proceeds unhindered. However, when a replication fork continues beyond the terminus, Tus–*Ter* is approached from the opposite direction (**Fig. 1a**), triggering it to form a tightly locked complex and bringing the replication fork to a halt[1,5–7]. Each *Ter* site is nonpalindromic, does not contain any direct repeats and has a strictly conserved G-C6 base pair followed by a highly conserved 13-bp core region. Tus is a monomeric protein that forms a simple 1:1 complex with *Ter*[8] (**Fig. 1b**). The structure of the Tus–*TerA* complex shows that many of the conserved residues among the *Ter* sites make base-specific contacts with the protein[4,9]. The Tus–*TerB* complex has a reported dissociation constant (K_d) of 44 pM in 50 mM NaCl[10]. This renders it the most stable complex known between a monomeric sequence-specific DNA-binding protein and a duplex-DNA recognition sequence.

A long-standing issue regards the manner in which the asymmetric blockage at Tus–*Ter* comes about. Does Tus itself function as a molecular roadblock, locking itself onto the *Ter* DNA as the DNA replication machinery approaches, or are there specific protein-protein interactions that lead to the polar arrest of the replisome? On one hand, various studies imply specific protein-protein interactions between Tus and the replicative helicase DnaB. Tus–*Ter* is much more effective in its natural host, for instance, while the functionally similar but structurally unrelated *Bacillus subtilis* replication termination system works well in *E. coli*[11,12]. Tus–*Ter* blocks DnaB, but not the Rep helicase, *in vitro*[13], and evidence from yeast two-hybrid analysis shows specific interactions between DnaB and Tus[14]. On the other hand, ample evidence suggests a protein-independent polar blocking mechanism. For example, RNA chain elongation catalyzed by T7, SP6 and *E. coli* RNA polymerases is impeded by Tus–*Ter* in a polar manner[15,16]. Tus–*TerB* also blocks the actions of the UvrD, Rep, PriA and SV40 large T antigen helicases, indicating low specificity for DnaB alone[17–20].

In 2006 light was shed on this molecular roadblock through a surface plasmon resonance (SPR) study of the dissociation of Tus from forked *TerB* oligonucleotides, which was supported by a crystal structure of a forked, 'locked' Tus–*Ter* complex[21]. This locked complex exhibits significant structural differences at the fork-blocking (nonpermissive) face in comparison with the ds*TerA*-bound, but not locked, Tus structure elucidated a decade earlier[4]. The locked conformation reveals that, of the single-stranded (ss) DNA bases in the forked *Ter* region (*Ter* bases 1–7), the highly conserved C6 base is flipped out of the helical DNA axis and into the protein (**Fig. 1c**). In this conformation the C6 base undergoes tight interactions with several amino acids (**Fig. 1d**). These Tus lock domain residues are distinctly different from those involved in sequence recognition and binding affinity[22]. It was therefore proposed that the Tus–*Ter* system is the molecular analog of a mousetrap: the trap is set by Tus binding to *Ter* in an oriented fashion and triggered by strand separation invoked by the approaching replication machinery[21].

The mousetrap model has two major implications. First, it suggests that binding and lock formation are two different mechanisms that can be ascribed to different domains of Tus. Second, lock formation through strand separation could occur independently of any specific protein-protein interactions. Nevertheless, convincing evidence arose that translocation of DnaB on double-stranded (ds) DNA in the absence of unwinding is sufficient to provoke polar arrest[23]. Although this result did not require it, these authors proposed an alternative model in which the DnaB helicase binds specifically to Tus. They argued that formation of the locked complex may act as a backup mechanism when protein-protein interaction fails but may not be sufficient on its own.

In this study, we used the quantitative power of high-throughput single-molecule approaches to address both of the key implications of the Tus–*Ter* mousetrap model and to dissect the overall mechanism of lock formation. By applying a mechanical force to unwind a DNA

[1]Department of Bionanoscience, Kavli Institute of Nanoscience, Delft University of Technology, Delft, the Netherlands. [2]Centre for Medical and Molecular Bioscience, University of Wollongong, Wollongong, Australia. [3]Present address: Biological Physics Research Group, Department of Physics, University of Oxford, Oxford, UK. *e-mail: n.h.dekker@tudelft.nl

hairpin containing a single *TerB* site, we mimicked replisome-mediated DNA unwinding and directly showed that strand separation alone could trigger the nonpermissively oriented Tus–*Ter* to form a strong and long-lived lock. Remarkably, the Tus–*Ter* lock formed in 100% of our hairpin-opening attempts. This was in contrast to Tus–*Ter* in the permissive orientation, where strand separation proceeded virtually unhindered. We quantified lock strength by measuring the lifetimes of the Tus–*Ter* complex at different forces. These experiments revealed that at high forces Tus dissociation occurred on three (or more) characteristic timescales, suggesting that strand separation at high forces partitioned the Tus–*Ter* structure into thermodynamically trapped substructures. We argue that the shorter-lived substructures correspond to intermediates in the process of full lock formation during replisomal strand separation and that the longest-lived structure is the full lock.

Our results strongly validated the molecular mousetrap model[21] by showing that Tus–*Ter* caused polar arrest of strand separation in the absence of any replication-related proteins. We showed that the interaction was efficient and was not limited by the rate of C6 flipping and finding the lock pocket. Using specific mutants we were able to discriminate DNA-binding and locking domains in this system. Residue H144, located deep in the Tus lock domain, determines the strength of interaction of the Tus–*Ter* lock: force-dependent lifetimes of H144A decreased more profoundly than those of any of the other single-site mutations tested. F140, located at the side of the lock pocket, was found to be involved in the specificity of the lock pocket for a C base. Notably, a mutation in residue E49, which is located outside the lock domain and thought to play a pivotal role in the specific interaction of Tus with DnaB, displayed a marked decrease in the probability of lock formation even though the lock lifetime was identical to that of wild-type (WT) Tus–*Ter*. This showed that E49 plays a crucial role in guiding C6 to the lock domain and that interfering with specific residues surrounding the Tus lock modulates the probability of forming a tightly locked Tus–*Ter* complex. Conversely, a mutation in the DNA-binding domain at the permissive face of the complex did not affect locking behavior. As *in vivo* experiments point toward probabilities of molecular-motor arrest substantially below those found here[12], we hypothesize that, instead of forming the basis of promoting polar arrest, protein-protein interactions may actually perform the opposite function of hindering proper lock formation. Our assay resolves the controversy that still surrounds this protein-DNA complex by providing direct insight into how different DNA processing enzymes in a head-on collision with Tus–*Ter* can exhibit varying blocking efficiencies, in particular by modulating the probability of lock formation through (nonspecific) steric hindrance.

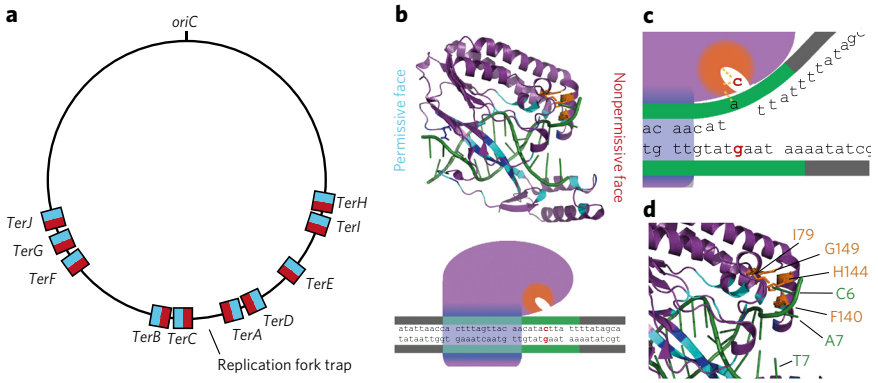

Figure 1 | The Tus–*Ter* complex structure and domains. (**a**) Location and orientation (turquoise for permissive face, red for nonpermissive face) of the 23-bp *Ter* sites in the *E. coli* chromosome. (**b**) The crystal structure (top) of the locked Tus–*Ter* complex (PDB ID: 2EWJ) with a schematic representation (bottom) showing the protein has a DNA-binding domain located mainly in the two antiparallel β-strands interacting with the major groove of *Ter* DNA (dark blue for base-specific interactions, light blue for nonspecific interactions). (**c**,**d**) Schematic representation (**c**) and crystal structure (**d**) showing the lock domain and amino acid residues (in orange) in Tus that interact specifically with C6 upon strand separation. In **d**, *Ter* nucleotides in green.

RESULTS

Mimicking replication fork progression using DNA hairpins

We set up a single-molecule assay using magnetic tweezers and DNA hairpins, which allowed us to controllably invoke the dsDNA unwinding that normally accompanies DNA replication, only now in the absence of the replication proteins. Our experiments initially comprised three DNA hairpin designs with specific sequences inserted at their midpoints: the first hairpin contained a single *TerB* site in the permissive orientation (**Fig. 2a**); the second had the *TerB* site inverted, forming the nonpermissive orientation (**Fig. 2b**); and lastly, the third hairpin contained a *TerB* site in the nonpermissive orientation, but included a point mutation at the G-C6 site in which the highly conserved C6 base was replaced by a guanine (referred to here as the 'GC flip') (**Supplementary Results**, **Supplementary Fig. 1b**). As the mousetrap model suggests a purely mechanical interaction for Tus–*Ter* upon strand separation, it predicts that, in our setup, lock formation should still occur in one direction (nonpermissive) but not the other (permissive). If protein-protein interactions are essential for proper lock formation, the phenomenon should, at most, be infrequent in our assay. We detected lock formation by measuring the difference in extension between a hairpin that is fully opened and one that is blocked halfway.

Tus–*Ter* blocks force-induced unwinding

At low forces (<16 pN), base-paired DNA is energetically more favorable than ssDNA, so the hairpin remains closed[24–26]. Upon increasing the force (>16 pN) in the absence of Tus, the hairpin opens, and this could be seen as a rapid increase in extension for both the permissive and the nonpermissive hairpins (**Fig. 2c**,**d**, red traces). Repeating this experiment in the presence of Tus resulted in an almost identical outcome for the permissive *Ter* hairpin (**Fig. 2c**, blue trace). Here the Tus–*Ter* interaction left only a transient signal upon hairpin opening (**Supplementary Fig. 2h**). In contrast, the results were very different for the nonpermissive hairpin (**Fig. 2d**, blue trace)—here the maximal extension in the presence of Tus was only half of the fully opened hairpin, indicating that strand separation was blocked exactly at the *Ter* site (see Online Methods and **Supplementary Fig. 1a**). This behavior was observed for nonpermissive hairpins in 100% of the experiments at 50 mM KCl and a Tus concentration of 2 nM. Increasing the ionic strength to 350 mM resulted in a modest decrease in the occurrence of blocking, but did not affect the lock strength (**Supplementary Fig. 2d**–**f**). The high efficiency of lock formation still occurred despite the fact that in our experiments the DNA helix was unwound at a rate of ~30 kbp/s (**Supplementary Fig. 1c**), which is at least tenfold faster than any replisome would unwind DNA. Increasing the force showed that the Tus–*Ter* lock could remain in place at forces up to 60 pN, demonstrating the remarkable strength of this locked complex. This experiment thus validated the proposed protein-protein independency[21] for fork arrest and strongly suggested that the Tus–*Ter* locking mechanism alone is readily equipped for the task of blocking an approaching replication fork, other helicases and the transcription machinery alike.

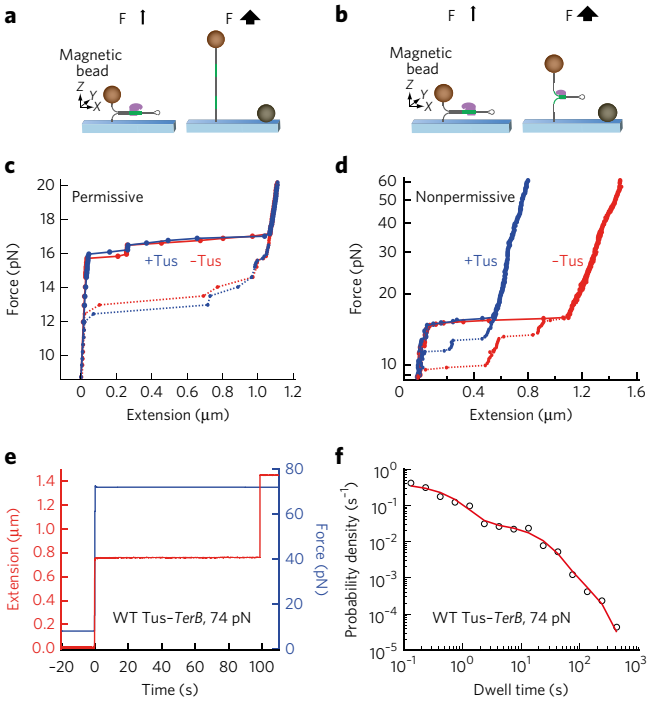

Figure 2 | Magnetic tweezers (MT) assay used to quantify the Tus–*Ter* lock mechanism. (**a**,**b**) Schematic overviews of a permissive (**a**) and a nonpermissive (**b**) Tus–*Ter* experiment. In the permissive experiment (**a**), force-induced DNA strand separation causes weakening of the interaction between the Tus DNA-binding domain and the *Ter* site, with subsequent disruption of the Tus–*Ter* interaction. (**b**) With the nonpermissively oriented *Ter* on a DNA hairpin, strand separation will cause the C6 base to flip into the high-affinity protein-binding pocket of Tus, resulting in a locked Tus–*Ter* complex. (**c**) Permissive MT DNA hairpin experiment yielding almost identical force extension curves for hairpins with (blue) or without (red) Tus, implying full opening of the hairpin. Dotted lines represent reannealing of the hairpin during force decrease. (**d**) Nonpermissive MT DNA hairpin experiment resulting in an extension that is halved in the presence of Tus (blue), suggesting that strand separation is blocked, compared to the same hairpin in the absence of Tus (red). (**e**) Quantification of lock behavior by measurement of lock dwell times under constant force. (**f**) Multiexponential distribution of dwell times (black circles) and fit of the kinetic model (red) (see text for explanation).

Lock breakage shows different degrees of lock formation

We measured the distribution of constant-force lock dwell times (**Fig. 2e**,**f**) for all protein and *Ter* variants (**Fig. 3a**) taking advantage of the natural force clamp mode and multiplexing capacity of magnetic tweezers. The distributions were highly reproducible and contained force-specific as well as mutant-specific signatures (**Fig. 3b**,**c** and **Supplementary Fig. 2a–c**). A main feature of all lock dwell time distributions was that they were (multi)exponentially distributed, reflecting the stochastic nature of lock rupture (**Fig. 2f**). We found that the distributions contained, according to the Bayes-Schwarz information criterion[27], two or three exponentially distributed states depending on the type of Tus–*Ter* interaction investigated. We used maximum-likelihood estimation to fit the data (**Fig. 2f**)[28] and obtained confidence intervals through bootstrapping[29] as described previously[30]. As these high-force measurements place a large tension on the DNA tethers, choosing the right force required a trade-off between tether lifetime[31] and the ability to resolve the different lock states (**Supplementary Fig. 1d**). Typically, we chose the force such that the three-exponential data sets exhibited a first short-lived exponential with a lifetime of ~1 s, a second exponential with a lifetime on the order of 10 s and a third, long-lived exponential on the order of 100 s.

In examining Tus locking behavior, it is convenient to consider this system through a lock-and-key analogy, where the C6 base is the key that fits into the Tus lock pocket (**Fig. 3a**). In this analogy, the interaction between WT Tus and nonpermissive *Ter* should provide a signature analogous to a perfect match between key and keyhole (**Fig. 3a**, WT Tus–*Ter*). We found the force-dependent dwell times of the WT Tus–*Ter* lock to be distributed over three states, with the longest-lived exponential distribution having a lifetime of ~720 s at 59 pN (**Fig. 3b**,**c**, purple circles). The shortest-lived exponential state at 59 pN had a lifetime of ~1 s, and the intermediate state had a lifetime of ~30 s. The lifetimes of all three states decreased in a concerted fashion as the force was increased, with the longest-lived distribution having a lifetime of 54 s at 93 pN (**Fig. 3c** and **Supplementary Table 1**). We also observed a force-dependent probability of forming the longest-lived state: although at 93 pN there was a mere 7% chance for a dwell time to belong to the longest-lived state, this probability increased to 73% at 59 pN (**Fig. 3d**,**e**). Conversely, trapping of the system in one of the shorter-lived states became progressively less likely as the force was decreased (**Supplementary Fig. 2i**). The force-dependent probability of all states also indicated that the first two states are likely to represent intermediate conformations that occur at all forces, while the longest-lived state represents the full lock. Thus when the magnetic tweezers exerted their highest forces, they prevented the short-lived conformations from proceeding to the fully locked state, while the longest-lived state predominated at low forces.

Experiments on permissive WT Tus–*Ter* resulted in sharply reduced dwell times that obeyed a single-exponential distribution with a mean of 0.8 s at 19 pN (**Fig. 3c** (purple square) and **Supplementary Fig. 2h**); at higher forces dwell times were too short to be detected. In fact, there was no single force at which both nonpermissive and permissive dwell times could be measured; the dwell times of nonpermissive WT Tus–*Ter* became too long at 19 pN for practical measurements (**Supplementary Fig. 1d**). This implies that none of the states we found for the nonpermissive orientation can be attributed solely to binding by Tus. To further investigate the origin of the observed states, we compared the changes in lifetime and probability invoked by mutations in Tus and/or *TerB*.

A binding-domain mutation does not hamper lock formation

The crystal structure of the locked WT Tus–*Ter* shows that DNA sequence recognition and binding can be largely attributed to a Tus DNA-binding domain that primarily consists of two antiparallel β-strands that interact with the major groove of *Ter* DNA (**Fig. 1b**). A site-specific mutation in the DNA-binding domain (Q250A, **Supplementary Fig. 3e**) is known to result in a sharp increase in the Tus–*TerB* K_d[22], but whether it affects lock kinetics is unknown. In our experiments, Q250A exhibited dwell time distributions very similar to those of WT Tus at the same forces (**Fig. 3c**, cyan). We saw no correlation between the K_d of Tus-ds*TerB* and lock strength. From this we concluded that lock formation is not severely affected by a change in Tus's DNA-binding domain.

C6 base is crucial but not rate-limiting for lock formation

We subsequently set out to examine the effect that changing the key (the C6 base) (**Fig. 3a**, switch from green to magenta key) had on WT Tus–*Ter* lifetimes. A single-base-pair inversion of the *TerB* sequence at position 6 profoundly affects the fork-arrest efficiency[32]. In our experiments inversion of G-C6 indeed had a dramatic effect on the lifetimes (**Fig. 3c**, purple triangles), as the dominant lifetime was no greater than 1 s at 40 pN. By comparison the dominant lifetime of WT Tus–*Ter* was at least two orders of magnitude higher, as indicated by extrapolation of the lifetimes of the fully locked state observed in the 59–93 pN range (**Fig. 3c**, purple circles). Despite

the decrease in observed lifetimes, the G6 *Ter* site continued to impose an increased barrier to hairpin opening because the lifetimes remained well above those found for binding of WT Tus only (**Fig. 3c**, purple square). For WT Tus with the modified key, we found two states (**Supplementary Fig. 2g**, purple), with the longest-lived lifetime decreasing from 39 to 0.7 s in the 29–40 pN range (**Fig. 3c**, purple triangles). We also assessed whether uncoupling lock formation from mechanical probing (by creating a hairpin with an unpaired region of five bases containing C6; see **Supplementary Figure 1b**) would populate the fully locked state even at high forces, as it is known that this 5-base mismatch dramatically increases the affinity of the Tus–*Ter* complex[21]. The resulting state probabilities, however, were identical to those of normal WT Tus–*Ter* (**Fig. 4a**), indicating that preformation of the lock did not alter the occupancy of the different states.

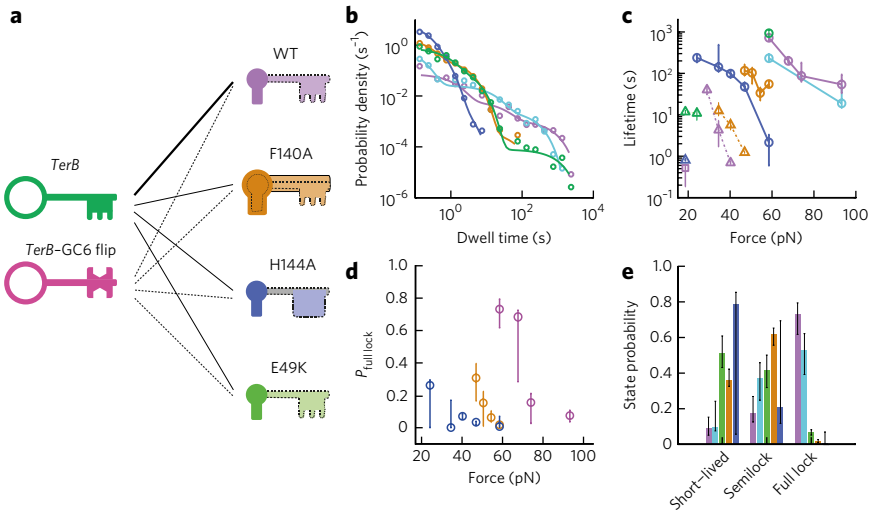

Figure 3 | The effect of Tus mutations on lock formation. (**a**) The Tus–*Ter* lock domains, depicted as keyholes, forming locked complexes with either *TerB* (green key) or *TerB* with a mutated GC6 bp (*TerB*-GC6 flip, magenta key). WT Tus (purple) and *TerB* are a perfect match, H144A (blue) is a mutation deep within the lock (blue, cavity behind keyhole becomes larger), F140A is a mutation at the edge of the lock pocket (orange, keyhole becomes larger) and E49K is a mutation that lies close to the lock domain (green, keyhole identical to WT). (**b**) The distribution of dwell times of WT Tus (purple, $N = 94$), the lock-domain mutants (H144A, blue, $N = 642$; F140A, orange, $N = 344$; E49K, green, $N = 323$) and binding-domain mutant Q250A (cyan, $N = 90$) when bound to *TerB* at 59 pN (circles are binned data, solid lines are fits). (**c**) The force-dependent lifetimes of the eight lock domain investigations depicted in **a**, as well as those of Q250A (cyan) and WT Tus in the permissive orientation (purple square). Lifetime of the longest-lived exponential is shown (see **Supplementary Table 1** for other lifetimes). Solid lines and circles are trends with *TerB*, while dashed lines and triangles are trends with *TerB*-GC6 flip. (**d**) The probability of entering the third, full-lock state (same color scheme as **c**). (**e**) The state-associated probabilities extracted (**Supplementary Results**, equations (1)–(4) and **Supplementary Table 2**) for all Tus species on *TerB* at 59 pN (purple, cyan, green, orange and blue bars represent WT, Q250A, E49K, F140A and H144A, respectively). In **c**–**e**, error bars represent the 1-σ confidence interval (CI).

Probing mechanism via mutations in or near the lock domain

To investigate how the *Ter* key enters the Tus lock, we performed experiments on a series of Tus mutants altered in or near the lock domain. Two amino acid residues, H144 and F140, are situated directly in the lock domain, and the crystal structure[21] suggests that their roles differ in a subtle, though significant, manner. Residue H144 lies deep within the lock pocket and interacts only with the C6 base. The H144A mutation removes the imidazole ring as well as a positive charge, leaving a cavity deep within the pocket (**Supplementary Fig. 3b**, in blue). In our lock-and-key representation, we depicted this by changing the inner shape of the lock (**Fig. 3a**, light blue). Amino acid residue F140 lies closer to the outer edge of the lock pocket than does H144. F140 still interacts with C6, and a stacking interaction of the phenyl ring with the adjacent A7 base is also present (**Supplementary Fig. 3c**, in orange). Removal of the phenyl ring in the F140A mutant would thus lead to a gap at the edge of the lock pocket, which we depict as a widening of the keyhole (**Fig. 3a**, orange). Residue E49, linked to the putative specific protein-protein interaction between Tus and the *E. coli* DnaB helicase[13,14], lies just outside the lock domain (**Supplementary Fig. 3d**, in green), although it does make a water-mediated hydrogen-bonding contact with the 5′ phosphate of A7 in the locked complex[21]. The shape of the lock pocket remained unaffected by this mutation (**Fig. 3a**, green keyhole identical to WT).

F140A affects specificity and H144A affects strength of the lock

We found that mutant F140A showed a marked decrease in dwell times at 59 pN (**Fig. 3b**, orange). Fitting revealed that the longest-lived exponential now had a lifetime of ~55 s, compared to 720 s for WT Tus at the same force (**Fig. 3c**, orange circles). We also observed that this third, longest-lived state had all but disappeared as the probability of entering this state was reduced from 73% for WT Tus to 1.8% for F140A in the same regime (**Fig. 3b** (orange; note the absence of counts >100 s) and **Fig. 3e** (orange bar in 'full lock' column)). Thus F140 appeared to give rise to the third, long-lived state observed in the Tus species with an intact lock pocket and, as such, seems to play a role in the probability of forming a fully locked state. Similarly to that of WT Tus, F140A's probability of attaining the full lock state exhibited a clear force-dependence: decreasing the force to 47 pN increased full lock probability to 31% (**Fig. 3d**, orange). Combining F140A with the mutated *Ter* site (**Fig. 3a**, magenta key with orange lock) further reduced the force-dependent lifetimes, but the resulting force-dependent lifetimes exceeded those of WT Tus with the mutated *Ter* site (**Fig. 3c** (orange triangles) and **Supplementary Fig. 2g**, orange circles). This apparent increase in lock strength in the presence of an altered key indicated that mutation of F140 led to a decreased specificity for allowing only the C6 base into the lock.

Replacing H144 led to a more substantial decrease in Tus–*Ter* lock dwell times than resulted from the F140A mutation (**Fig. 3b**,**c**, blue circles). The dominant lifetime extracted at 59 pN was found to be ~2 s, whereas those of WT Tus and Q250A at the same force were two orders of magnitude higher. The data sets were found to exhibit lifetimes measurable over a wide range of forces (24–59 pN), and all retained three exponential states. At 59 pN, H144A led to a larger drop in the probability of entering the third, longest-lived state than that for F140A, from 73% for WT Tus to 0.7% for H144A (**Fig. 3e**, blue). As observed for F140A and WT Tus, there was also a clear force-dependence in the probability to form a fully locked state for H144A: the probability increased to 26% at 24 pN (**Fig. 3d**, blue line). While H144A is the single-site mutation with the greatest effect on lock lifetimes, the decrease was not as severe as that for WT Tus with the G6 *Ter* site. When combining the H144A lock mutant with the mutated *Ter* site (**Fig. 3a**, magenta key with blue lock),

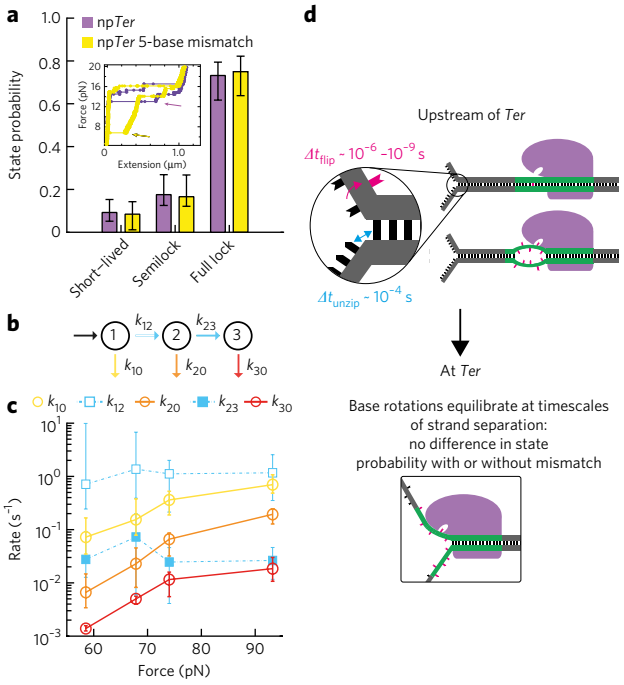

Figure 4 | Modeling Tus–*Ter* lock formation and extracting state-associated rates and probabilities. (**a**) State probabilities extracted through fitting the dwell time distributions at 59 pN for WT Tus–*Ter* (purple, same data as **Fig. 3e**) and WT Tus on the *Ter* site containing the mismatched bases 3–7 (yellow). Inset, the force-extension curves of both types of hairpins showing that the force at which the mismatch hairpin returns to its fully closed state (yellow arrow, ~7 pN) consistently lies in the entropic regime (i.e., the forces at which ssDNA is no longer fully stretched), whereas the closing force lies markedly higher than the entropic regime for the normal hairpin (purple arrow, ~13 pN). Np, nonpermissive. Error bars indicate 1-σ confidence intervals. (**b**) The 3-state kinetic model used to fit the data sets (**Supplementary Fig. 4**). (**c**) The force-dependent trends in the kinetic rates extracted by fitting the exponential states of WT Tus–*Ter* (**Supplementary Results**, equations (5)–(7) and **Supplementary Table 2**). We observed an exponential increase in all state exit rates (k_{10}, k_{20}, k_{30}, represented by yellow, orange and red, respectively) with increasing force, while the rates connecting states 1 and 2 (cyan) as well as states 2 and 3 (cyan, fill) remain roughly constant (error bars indicate 1-σ confidence intervals). (**d**) Schematic representation of the estimated rate of base flipping versus the rate of base pair unwinding in our experiments for the normal *Ter* hairpin and the *Ter* site containing a mismatch region. The identical probability distributions for WT Tus–*Ter* and WT Tus on *Ter* with five mismatched bases shown in **a** are a result of the much faster process of base flipping compared to strand separation.

the resulting distribution (0.5 s at 19 pN; **Fig. 3c**, blue circle) was not unlike that obtained for permissively oriented WT Tus (0.8 s at 19 pN) (**Supplementary Fig. 2h**, blue circles). This indicated that H144A–WT *Ter* lifetimes result from the specific interactions of the C6 base with the remaining amino acid residues in the lock pocket, and that further modification of the key within this altered lock result in the loss of all locking interactions.

E49K decreases the probability of lock formation

For E49K we obtained a distribution of dwell times at 59 pN that contained the same three exponentially distributed states as WT Tus–*Ter* (**Fig. 3b**, green circles), with a longest-lived state lifetime of 933 s (720 s for WT). However, the probability of this state decreased markedly from 73% for WT to 6% for E49K (**Fig. 3e**). The first two exponentials fully overlapped with the two shortest-lived ones for F140A (**Fig. 3b**, orange circles). This suggested that the DNA-phosphate interaction with E49 is crucial for guiding the C6 base into the Tus lock pocket to form the fully locked state. Mutating the *TerB* site (**Fig. 3a**, magenta key with green lock) caused a loss of almost all dwell times above ~1 s for forces above 26 pN, similar to the barrier imposed by Tus–*Ter* in the permissive orientation (**Supplementary Fig. 2g**). However, closer inspection revealed longer-lived events with a low probability of ~1.5% (**Supplementary Fig. 2h** and **Supplementary Table 2**). When extrapolated to higher forces, the longer lifetimes (**Fig. 3c**, green triangles) resembled the much more probable states found for the interaction between WT Tus and the mutated *Ter* site in the 29–40 pN range (**Fig. 3c**, purple triangles, and **Supplementary Table 2**). This indicated that while the WT lock domain continued to interact with the incorrect G6 key, mutation of E49 rendered such an interaction unlikely. Our observations clearly link the change invoked by E49K to a change in the probability of forming the third, fully locked state.

On the basis of our observations, we propose a kinetic model for WT lock formation involving three states (**Fig. 4b** and **Supplementary Fig. 4**). In this model, the Tus–*Ter* complex strengthens progressively and irreversibly upon passage from one stable state to the next until the final, fully locked and longest-lived state is reached. Fitting this kinetic model to the data revealed that loss of the long-lived lock state as the force is increased is not due to slower transitions to stronger lock states (**Fig. 4c**, k_{12} and k_{23}) but rather to increased rates of disruption (k_{10}, k_{20} and k_{30}) of the lock states, as the force-dependent trends in these rates showed.

DISCUSSION

Our results have important implications for understanding of how the Tus–*Ter* lock is formed. We can directly discard the notion that Tus–*Ter* requires specific interaction with DnaB to form a stable lock and block replication fork progression for extended times. Our results strongly suggest that strand separation followed by specific interaction of the *Ter* C6 base with the Tus lock domain is the only mechanism needed for polar arrest. Evidence for this can be found in the fact that lock probabilities and lifetimes are affected by mutations in the lock domain or by mutation of the C6 base, but not by a mutation in the DNA-binding domain. We further observed that mutant E49K, which is hypothesized to be deficient in polar replication-fork arrest due to the elimination of specific protein-protein interactions[13,14], gave rise to lifetimes identical to that of WT Tus, only now with a severely decreased probability of entering the longest-lived state. This tied the observed deficiency of *in vivo* fork arrest to the decrease in occurrence of the longest-lived state found in our experiments. In other words, the longest-lived state is likely to be the native lock conformation implicated in *in vivo* fork arrest, and we showed residue E49 to be part of the mechanism that facilitates formation of a tight interaction between C6 and the lock pocket.

Our experiments also demonstrated that the flipping of the C6 base and *Ter*'s subsequent interactions with the Tus lock pocket is not a rate-limiting step in the lock formation process. This is supported by our observation that there was little force-dependence in the inter-state rates (k_{12} and k_{23}) (**Fig. 4b**,**c**); this means that the force-dependence of state probabilities was caused solely by the force-dependent state exit rates (k_{10}, k_{20} and k_{30}). As force influences the speed of strand separation and thus the time available for C6 flipping while not affecting the inter-state transfer rates, the C6 flipping is likely not rate limiting at the comparatively low unwinding velocities (**Supplementary Fig. 1c**) of the *E. coli* replisome.

This notion is further strengthened by our observation that preformation of the lock yielded a distribution of dwell times identical to those of normal Tus–*Ter* (**Fig. 4a**). In the preformed lock situation, it could be assumed that the C6 base has reached its equilibrium lock position. Our results imply that our pulling

experiment provided sufficient time for this equilibration, although the pulling experiment as a whole is a system in nonequilibrium. This can be directly understood by comparing the typical timescales of DNA unwinding and the timescale of molecular rearrangement of the DNA bases upon disruption of Watson-Crick base pairing (**Fig. 4d**). The unwinding rate of DNA by a replisome is of the order of 1 kbp/s, and in our pulling experiments this rate is ~30 kbp/s. Typical molecular single-bond rotations are known to take place on femtosecond to picosecond timescales, with larger-scale motions such as lock formation likely occurring in the nanosecond to microsecond range[33–35]. This implies that there is at least several orders of magnitude of difference between the rate of unwinding and the rate at which flipping of C6 and concomitant molecular rearrangements take place, leaving ample time for C6 to reach its equilibrium-locked conformation.

The interpretation that the longest-lived state is the native, or full lock, state implies the probability of native lock formation is substantially lower than 100% at the highest forces measured (**Fig. 3d**, purple). The force-dependent lock probabilities do, however, suggest that the full lock is the dominant state at low forces for WT Tus, and suggest that the mutant with the lowest full-lock probability (H144A) might still have a significant chance of blocking an approaching replisome. Identifying a more direct link between our probabilities and *in vivo* arrest efficiencies would require knowledge of, for example, the amount of work performed by a replisome. It remains to be determined to what extent the two shortest-lived lock states are capable of causing arrest of DNA-processing enzymes, although the reported replisome arrest deficiency of E49K[13,14] and our observation that E49K affected only the longest-lived state suggest that these intermediate states are not sufficient to block replication fork progression. It is clear, though, that these two 'lesser' lock states still pose a significant barrier to strand separation, much more so than the mere binding of Tus alone.

The difference between the high efficiency of reaching the full-lock state that we observed and the lower efficiencies of replisome arrest observed *in vivo*[12] must have a cause arising from interactions not captured in our experiments. These interactions might be invoked by the presence of an enzyme running into Tus–*Ter*, and steric effects (through functional protein-protein interactions) could then be the cause of the observed decrease in efficiency. Thus, instead of providing the basis of fork arrest, functional interactions could have an antagonistic effect *in vivo*. Our experiments with mutant E49K suggested a possible mechanism: just as the mutation in the Tus protein modulates the probability of forming the fully locked state without affecting the lifetime of the lock, an enzyme running into Tus–*Ter* could invoke a similar effect through functionally interacting with that same residue. Our experiments with WT and E49K Tus, respectively, thus set the upper (no interaction, high lock probability) and lower (E49 function completely disrupted, low lock probability) boundaries of blocking probabilities. Two different enzymes that run into nonpermissive Tus–*Ter* could then, in turn, have their own characteristic probabilities of being blocked due to the their differential modes of nonspecific interaction with Tus residues (such as E49) upon collision.

Received 23 November 2014; accepted 20 May 2015;
published online 6 July 2015

METHODS

Methods and any associated references are available in the online version of the paper.

References

1. Hill, T.M., Henson, J.M. & Kuempel, P.L. The terminus region of the *E. coli* chromosome contains two separate loci that exhibit polar inhibition of replication. *Proc. Natl. Acad. Sci. USA* **84**, 1754–1758 (1987).
2. Hidaka, M., Kobayashi, T., Takenaka, S., Takeya, H. & Horiuchi, T. Purification of a DNA replication terminus (*ter*) site–binding protein in *Escherichia coli* and identification of the structural gene. *J. Biol. Chem.* **264**, 21031–21037 (1989).
3. Hill, T.M. Arrest of bacterial DNA replication. *Annu. Rev. Microbiol.* **46**, 603–633 (1992).
4. Kamada, K., Horiuchi, T., Ohsumi, K., Shimamoto, N. & Morikawa, K. Structure of a replication-terminator protein complexed with DNA. *Nature* **383**, 598–603 (1996).
5. Khatri, G.S., MacAllister, T., Sista, P.R. & Bastia, D. The replication terminator protein of *E. coli* is a DNA sequence-specific contra-helicase. *Cell* **59**, 667–674 (1989).
6. Hill, T.M. & Marians, K.J. *Escherichia coli* Tus protein acts to arrest the progression of DNA replication forks *in vitro*. *Proc. Natl. Acad. Sci. USA* **87**, 2481–2485 (1990).
7. Hill, T.M. in *Escherichia coli and Salmonella: Cellular and Molecular Biology* 2nd edn. (eds. Neidhardt, F.C. *et al.*) 1602–1614 (American Society for Microbiology, Washington, DC, USA, 1996).
8. Coskun-Ari, F.F., Skokotas, A., Moe, G.R. & Hill, T.M. Biophysical characteristics of Tus, the replication arrest protein of *Escherichia coli*. *J. Biol. Chem.* **269**, 4027–4034 (1994).
9. Neylon, C., Kralicek, A.V., Hill, T.M. & Dixon, N.E. Replication termination in *Escherichia coli*: structure and anti-helicase activity of the Tus-*Ter* complex. *Microbiol. Mol. Biol. Rev.* **69**, 501–526 (2005).
10. Lee, J.Y., Finkelstein, I.J., Arciszewska, L.K., Sherratt, D.J. & Greene, E.C. Single-molecule imaging of FtsK translocation reveals mechanistic features of protein-protein collisions on DNA. *Mol. Cell* **54**, 832–843 (2014).
11. Kaul, S. *et al.* The replication terminator protein of the gram-positive bacterium *Bacillus subtilis* functions as a polar contrahelicase in gram-negative *Escherichia coli*. *Proc. Natl. Acad. Sci. USA* **91**, 11143–11147 (1994).
12. Andersen, P.A., Griffiths, A.A., Duggin, I.G. & Wake, R.G. Functional specificity of the replication fork-arrest complexes of *Bacillus subtilis* and *Escherichia coli*: significant specificity of Tus-*Ter* functioning in *E. coli*. *Mol. Microbiol.* **36**, 1327–1335 (2000).
13. Sahoo, T., Mohanty, B.K., Lobert, M., Manna, A.C. & Bastia, D. The contrahelicase activities of the replication terminator proteins of *Escherichia coli* and *Bacillus subtilis* are helicase-specific and impede both helicase translocation and authentic DNA unwinding. *J. Biol. Chem.* **270**, 29138–29144 (1995).
14. Mulugu, S. *et al.* Mechanism of termination of DNA replication of *Escherichia coli* involves helicase-contrahelicase interaction. *Proc. Natl. Acad. Sci. USA* **98**, 9569–9574 (2001).
15. Mohanty, B.K., Sahoo, T. & Bastia, D. The relationship between sequence-specific termination of DNA replication and transcription. *EMBO J.* **15**, 2530–2539 (1996).
16. Mohanty, B.K., Sahoo, T. & Bastia, D. Mechanistic studies on the impact of transcription on sequence-specific termination of DNA replication and vice versa. *J. Biol. Chem.* **273**, 3051–3059 (1998).
17. Lee, E.H., Kornberg, A., Hidaka, M., Kobayashi, T. & Horiuchi, T. *Escherichia coli* replication termination protein impedes the action of helicases. *Proc. Natl. Acad. Sci. USA* **86**, 9104–9108 (1989).
18. Lee, E.H. & Kornberg, A. Features of replication fork blockage by the *Escherichia coli* terminus-binding protein. *J. Biol. Chem.* **267**, 8778–8784 (1992).
19. Bedrosian, C.L. & Bastia, D. *Escherichia coli* replication terminator protein impedes simian virus 40 (SV40) DNA replication fork movement and SV40 large tumor antigen helicase activity *in vitro* at a prokaryotic terminus sequence. *Proc. Natl. Acad. Sci. USA* **88**, 2618–2622 (1991).
20. Hidaka, M. *et al.* Termination complex in *Escherichia coli* inhibits SV40 DNA replication in vitro by impeding the action of T antigen helicase. *J. Biol. Chem.* **267**, 5361–5365 (1992).
21. Mulcair, M.D. *et al.* A molecular mousetrap determines polarity of termination of DNA replication in *E. coli*. *Cell* **125**, 1309–1319 (2006).
22. Neylon, C. *et al.* Interaction of the *Escherichia coli* replication terminator protein (Tus) with DNA: a model derived from DNA-binding studies of mutant proteins by surface plasmon resonance. *Biochemistry* **39**, 11989–11999 (2000).
23. Bastia, D. *et al.* Replication termination mechanism as revealed by Tus-mediated polar arrest of a sliding helicase. *Proc. Natl. Acad. Sci. USA* **105**, 12831–12836 (2008).
24. Liphardt, J., Onoa, B., Smith, S.B., Tinoco, I. Jr. & Bustamante, C. Reversible unfolding of single RNA molecules by mechanical force. *Science* **292**, 733–737 (2001).
25. Woodside, M.T. *et al.* Nanomechanical measurements of the sequence-dependent folding landscapes of nucleic acid hairpins. *Proc. Natl. Acad. Sci. USA* **103**, 6190–6195 (2006).

26. Lionnet, T., Spiering, M.M., Benkovic, S.J., Bensimon, D. & Croquette, V. Real-time observation of bacteriophage T4 gp41 helicase reveals an unwinding mechanism. *Proc. Natl. Acad. Sci. USA* **104**, 19790–19795 (2007).
27. Schwarz, G. Estimating dimension of a model. *Ann. Statist.* **6**, 461–464 (1978).
28. Cowan, G. *Statistical Data Analysis* (Oxford University Press, Oxford, UK, 1998).
29. Press, W.H., Flannery, B.P., Teukolsky, S.A. & Vetterling, W.T. *Numerical Recipes in C: The Art of Scientific Computing* 2nd edn. (Cambridge University Press, Cambridge, UK, 1992).
30. Dulin, D. *et al.* Elongation-competent pauses govern the fidelity of a viral RNA-dependent RNA polymerase. *Cell Rep.* **10**, 983–992 (2015).
31. Janissen, R. *et al.* Invincible DNA tethers: covalent DNA anchoring for enhanced temporal and force stability in magnetic tweezers experiments. *Nucleic Acids Res.* **42**, e137 (2014).
32. Coskun-Ari, F.F. & Hill, T.M. Sequence-specific interactions in the Tus-*Ter* complex and the effect of base pair substitutions on arrest of DNA replication in *Escherichia coli*. *J. Biol. Chem.* **272**, 26448–26456 (1997).
33. Dantus, M., Bowman, R.M. & Zewail, A.H. Femtosecond laser observations of molecular vibration and rotation. *Nature* **343**, 737–739 (1990).
34. Arasaki, Y., Takatsuka, K., Wang, K. & McKoy, V. Energy- and angle-resolved pump-probe femtosecond photoelectron spectroscopy: molecular rotation. *J. Chem. Phys.* **114**, 7941–7950 (2001).
35. Middleton, C.T. *et al.* DNA excited-state dynamics: from single bases to the double helix. *Annu. Rev. Phys. Chem.* **60**, 217–239 (2009).

Acknowledgments

We thank J. Cnossen for his countless efforts in adjusting the MT software to our needs, J. Kerssemakers for discussions and S. Hamdan for his contribution to the discussion by generously sharing his own experimental observations. This study was supported by a grant from the Australian Research Council (DP0877658) to N.E.D. and by Vici and TOP grants from the Netherlands Organisation for Scientific Research (NWO) and ERC Starting Grant DynGenome from the European Research Council to N.H.D.

Author contributions

N.E.D. and N.H.D. designed the research. B.A.B. and N.H.D. designed the experiments. D.D. designed and assembled the magnetic tweezers apparatus. B.A.B. performed the experiments. B.A.B., B.C., T.v.L., R.J. and N.H.D. designed, and B.C. and T.v.L. made, the DNA hairpin constructs. Z.-Q.X. and S.J. purified the Tus proteins. B.A.B. and M.D. analyzed the data. M.D. developed the application of MLE to force spectroscopy data. B.A.B., D.D., M.D. and N.H.D. interpreted the data. S.J. and N.E.D. contributed to discussions concerning the model and *in vivo* observations. B.A.B., N.E.D. and N.H.D. wrote the paper.

Competing financial interests

The authors declare no competing financial interests.

Additional information

Supplementary information, chemical compound information and chemical probe information is available in the online version of the paper. Reprints and permissions information is available online at http://www.nature.com/reprints/index.html. Correspondence and requests for materials should be addressed to N.H.D.

ONLINE METHODS

DNA hairpins. Plasmids pTER and pTER_Rev, containing the *TerB* site in either the nonpermissive or permissive orientation, respectively, and flanked by phage λ sequences, were obtained from Invitrogen. Plasmid pTER_mutant, encoding mutated *TerB* (C6→G6) was generated from pTER by site-directed mutagenesis using primers 1 and 2 (primer sequences are in listed in the next paragraph). Hairpins were constructed in a multistep process (**Supplementary Fig. 1**). First, 1-kb fragments containing the *TerB* site were amplified from the three pTER plasmids using primers 3 and 4. These fragments were digested with the nonpalindromic restriction enzyme BsaI (New England BioLabs Inc., Ipswich, MA) and ligated at one end with a 42-bp oligonucleotide to form a U-turn (oligonucleotide 5). To create a 1-kb fragment containing a 5-base mismatch between bases 3–7 in the *Ter* site, two fragments of 500 bp were generated by PCR using pTER as template and primer combinations 3 and 12 and 4 and 13, respectively. These fragments were digested with BsaI and ligated to each end of the annealed primer pair 14 and 15 containing the wobble. Hairpin handles were created by PCR amplification of a 1.2-kb pBluescript SK+ (Stratagene–Agilent Technologies, Santa Clara, CA) fragment using primers 6 and 7 in the presence of either biotin-16-dUTP or digoxigenin-11-dUTP (Roche Diagnostics, Basel, Switzerland). Prior to ligation to spacer oligonucleotides, handles were digested with either BamHI or NotI. The upper spacer of the hairpin was generated by annealing 5′-phosphorylated oligonucleotides 8 and 9 and ligating this double-stranded DNA fragment to the NotI-digested biotin-labeled handle. The lower spacer was made by annealing 5′-phosphorylated primers 10 and 11 and ligating them to the BamHI-digested digoxigenin-labeled handle. Finally, the overhangs of these handle-spacer constructs were allowed to anneal to form a short (50-bp) stem with a 5′-GCAA overhang that was ligated to the complementary BsaI site of the 1-kb *TerB* fragment. Oligonucleotides were obtained from Biolegio B.V., Nijmegen, the Netherlands and from Ella Biotech GmbH, Martinsried, Germany.

Primers. Sequences of primers for PCR amplifications and oligonucleotides that contribute to the structure of the hairpin were as follows: primer 1, 5′-CACCA CGACTGTGCTATAAAATAACTATGTTGTAACTAAAGTGGTTAATAT-3′; primer 2, 5′-ATATTAACCACTTTAGTTACAACATAGTTATTTTATAGCAC AGTCGTGGTG-3′; primer 3, 5′-CTGCGGTCTCGTTGCTTACCGTCACCA GAAATTACCGTCAC-3′; primer 4, 5′-CCATCTTGGTCTCCTAGGTTTTTA GCAGCGAAGCGTTTGATAAG-3′; primer 5, 5′-CCTAAGCTCGCCGAGG CGAGCGAAAGCTCGCCTCGGCGAGCT-3′; primer 6, 5′-GACCGAGAT AGGGTTGAGTG-3′; primer 7, 5′-CAGGGTCGGAACAGGAGAGC-3′; primer 8, 5′-GGCAAGAGCAACTCGGTCGCCGCATACACTATTCTCAGAATGAC TTGGTT-3′; primer 9, 5′-GGCCAACCAAGTCATTCTGAGAATAGTGTATG CGGCGACCGAGTTGCTCTTGCCATGCTCTTTACAACCGG TTGACTGCTTCAGGGGTCGATCCCGCTTTGTAC-3′; primer 10, 5′-GATC TCGTTCATCCATAGTTGCCTGACTCCCCGTCGTGTAGAT AACTACGATACGGGAGGGCTTACCATCTGGC-3′; primer 11, 5′-GCAA GTACAAAGCGGGATCGACCCCTGAAGCAGTCAA CCGGTTGTAAAGAGCATCGATCGTTGTCAGAAGTAAGTTGGC CGCAGTGTTATCACTCATGGTTATGCCAGATGGTAAGCCCTC CCGTATCGTAGTTATCTACACGACGGGGAGTCAGGCAA CTATGGATGAACGA-3′; primer 12, 5′-CCATCTTGGTCTCCGACATTAT AGCACAGTCGTGGTGAC-3′; primer 13, 5′-CTGCGGTCTCGAGGCGGT TAATATTATGGCGCGTTG-3′; primer 14, 5′-P-GCCTACTTTAGTTACAA CATACTTATT-3′; primer 15, 5′-P-TGTCAAACCTCATGTTGTAACTAAAGT-3′.

Tus proteins. N-terminally His_6-tagged Tus and mutant derivatives were prepared as described[21,22]; their concentrations were determined spectrophotometrically (ε_{280} = 39,700 $M^{-1}cm^{-1}$).

Magnetic tweezers—experimental configuration. The magnetic tweezers implementation used in this study has been described[30,31,36]. In short, light transmitted through the sample was collected by an oil-immersion objective (Olympus UPLSAPO60XO 60×, numerical aperture (NA) = 1.35, Olympus, USA) and projected onto a 12-megapixel CMOS camera (Falcon FA-80-12M1H, Teledyne Dalsa, Canada) with a sampling frequency of 58 Hz at full field of view, or higher when cropped. A 2-inch 200-mm tube lens between objective and camera made the effective magnification 67×. The applied magnetic field was generated by a pair of vertically aligned permanent neodymium-iron-boron magnets (SuperMagnete, Switzerland) separated by a distance of 1.0 or 0.5 mm and suspended on a motorized stage (M-126.PD2, Physik Instrumente, Germany) above the flow cell. Additionally, the magnet pair could be rotated about the illumination axis by an applied DC servo step motor (C-150.PD, Physik Instrumente, Germany).

Data processing. Image processing of the collected light was used to track the real-time position of both surface-attached reference beads and superparamagnetic beads coupled to DNA tethers in three dimensions. We implemented custom written software in C++, CUDA and LabView (2011, National Instruments Corporation, USA) that is suited for high-throughput tracking in magnetic tweezers[36]. In short, tracking of the *x,y* coordinates is performed using center-of-mass computation followed by a further refinement using the quadrant interpolation algorithm. Localization of the bead's *z*-coordinate is achieved by creating a radial profile using the refined *x,y* coordinates and comparing this profile to a prerecorded LUT of radial profiles. After subtraction of the reference bead position to correct for instrumental drift, the *x*, *y* and *z* positions of the DNA-tethered beads were determined with a spatial accuracy of <3 nm. The upward stretching forces on the DNA tethers by the superparamagnetic beads were calibrated from analysis of the extent of its Brownian motion whereby spectral corrections were employed to correct for camera blur and aliasing[37,38].

Sample preparation and data acquisition. The sample preparation used in this study has been described in detail elsewhere[31]. In short, the DNA hairpins (final concentration ~50 pg/µl) were mixed and incubated for 2 min with 20 µl streptavidin-coated paramagnetic polystyrole beads (M270 Dynabeads) at room temperature in Tris buffer (50 mM Tris-HCl pH 7.9, 50 mM KCl, 0.1 mM EDTA, 0.01% Triton X-100). The supernatant was replaced by 50 µl Tris buffer followed by a 15 min incubation of the bead-DNA solution in the flow cell containing an anti-digoxigenin–coated nitrocellulose surface. Nontethered beads were removed by flushing with 1 ml Tris buffer, applying a high (30–40 pN) force while rotating the magnets (10 r.p.m.), and followed by flushing with more buffer until all nontethered beads had been flushed out. All KCl buffers used in this study exclusively contained 50 mM Tris-HCl pH 7.9, 0.1 mM EDTA, 0.01% Triton X-100 unless noted otherwise. Tus proteins were diluted 1,000-fold from stock (to ~10 nM) unless high salt concentrations required higher concentrations. Data were acquired at 100 Hz with a 10-ms acquisition time. Force-extension curves were obtained through changing the magnet position in an exponential fashion such that the force change was linear. Constant-force dwell time experiments were obtained by lowering the magnets in a linear fashion (10 mm/s) to the desired distance. The dwell time is the time measured between arrival of the magnets at their final position and the further opening of the hairpin from the locked to the fully opened state.

Data analysis and statistical procedure. Rupture of the Tus–*Ter* lock results in a sudden opening of the DNA hairpin: rupture points were easily identified as a sharp peak in the derivative of the *z*-trace. The dwell-time distribution

$$P(t) = \sum_{n=1}^{M} A_n e^{-k_n t} \tag{1}$$

with M number of exponentials (as determined by the Bayes–Schwarz information criterion[27]) is fit to the data set containing N experimentally collected dwell times $\{t_i\}_i$ by minimizing the likelihood function[28]

$$L = -\sum_{i=1}^{N} \ln P(t_i) \tag{2}$$

with respect to rates and probabilistic weights (**Supplementary Results**, equations (2) and (3)). We calculated the errors in our parameter estimates by bootstrapping the system 1,000 times, and reported the one-sigma confidence intervals (1-σ CI) among the bootstrapped data sets (**Supplementary Tables 1** and **2**).

36. Cnossen, J.P., Dulin, D. & Dekker, N.H. An optimized software framework for real-time, high-throughput tracking of spherical beads. *Rev. Sci. Instrum.* **85**, 103712 (2014).
37. te Velthuis, A.J., Kerssemakers, J.W., Lipfert, J. & Dekker, N.H. Quantitative guidelines for force calibration through spectral analysis of magnetic tweezers data. *Biophys. J.* **99**, 1292–1302 (2010).
38. Yu, Z. *et al.* A force calibration standard for magnetic tweezers. *Rev. Sci. Instrum.* **85**, 123114 (2014).

doi:10.1038/nchembio.1857

Supplementary Information for:

Strand separation establishes a sustained lock at the Tus–*Ter* replication fork barrier

Bojk A. Berghuis[1], David Dulin[1], Zhi-Qiang Xu[2], Theo van Laar[1], Bronwen Cross[1], Richard Janissen[1], Slobodan Jergic[2], Nicholas E. Dixon[2], Martin Depken[1] & Nynke H. Dekker[1*]

[1]Department of Bionanoscience, Kavli institute of Nanoscience, Delft University of Technology, Lorentzweg 1, 2628 CJ Delft, The Netherlands

[2]Centre for Medical and Molecular Bioscience and School of Chemistry, University of Wollongong, New South Wales 2522, Australia

* Correspondence may be addressed to n.h.dekker@tudelft.nl.

Supplementary Results

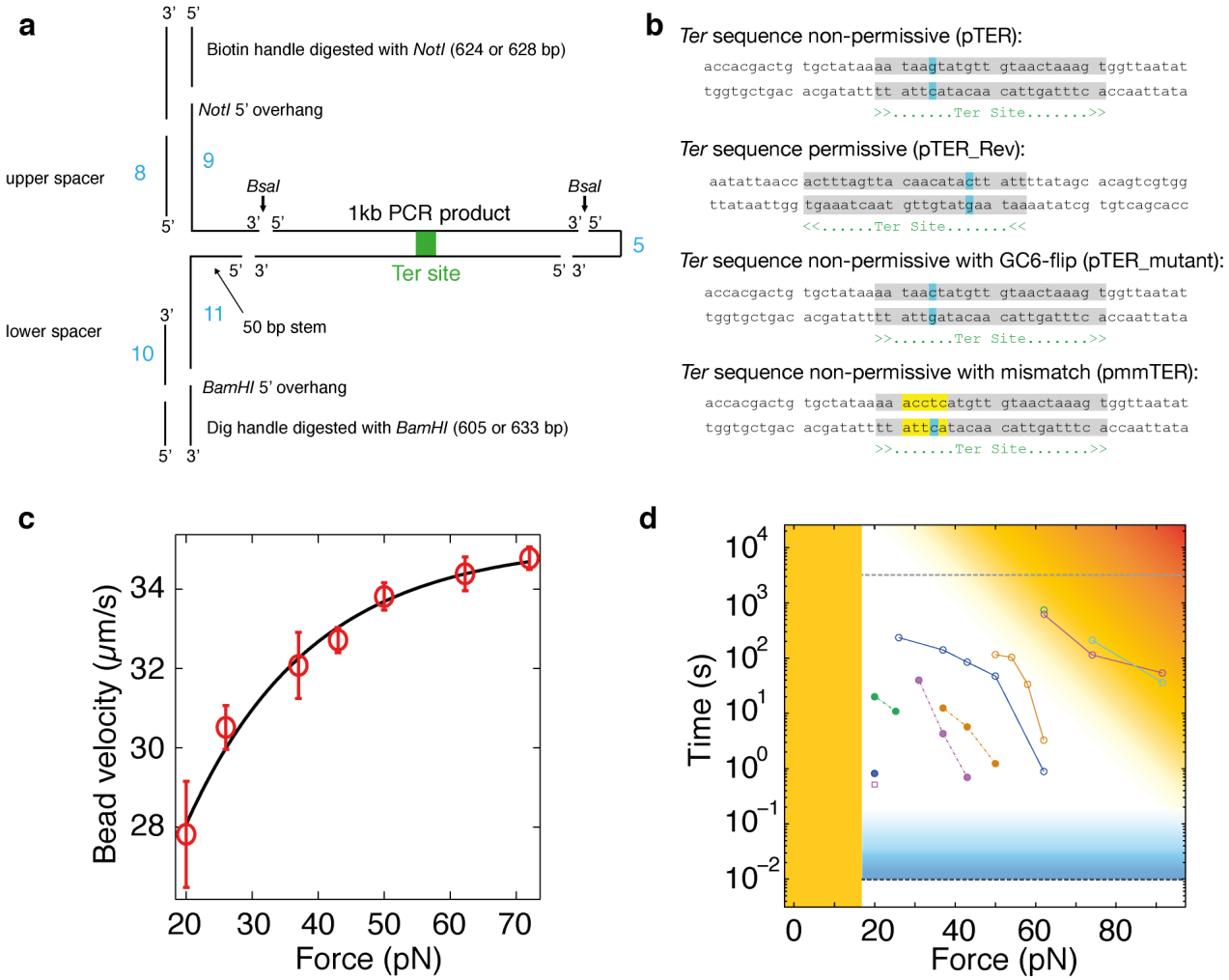

Supplementary Figure 1. DNA hairpin design and characteristics. **(a)** The DNA hairpin construct made as described in the **Online Methods**. (**b**) The used *Ter* sequences. **(c)** Velocity versus force profile of a hairpin opening in the magnetic tweezers. We compute velocities by determining the maximum value of the central

Nature Chemical Biology: doi:10.1038/nchembio.1857

derivative of the extension versus time traces, i.e. the instantaneous apparent velocity upon lock rupture. Each data point in the figure is the average of hundreds of rupture events (the data here are from ~10^4 rupture events). The data have been fit with a single exponential (black line) to provide a guide to the eye. Note that our computations only provide a lower bound to the velocity, since our 100 Hz sampling frequency is not sufficiently high to capture the opening dynamics over a typical distance of ~0.6 μm (500 bp opening). Nonetheless, these lower bounds suffice to indicate that the hairpin-opening rate exceeds the DNA unwinding rate of the *E. coli* replisome by at least 10-fold at 20 pN force. **(d)** Here we visualize the constraints on the experimental time–force window due to biological (orange) or instrumentation (blue) limits. The data, identical to Figure 3c, is added as a frame of reference. Below ~16 pN, base-paired DNA is energetically more favorable, therefore the hairpin remains closed (orange fill). With an acquisition rate of 100 Hz, the cutoff time is in principle 10^{-2} s (black dashed line); however, the error already becomes relatively large for lock lifetimes shorter than 0.1 s (blue gradient). Measurements are further limited by the lifetime of the DNA hairpin since DNA tethering relies on electrostatic interactions. This implies that very long measurement times, high forces or a combination of both (orange gradient) should be avoided. Typically we avoided having to measure lifetimes exceeding an hour (grey dashed line). Here we are able to see that the force–lifetime behavior exhibited by wt Tus already approaches the limits of the assay.

Nature Chemical Biology: doi:10.1038/nchembio.1857

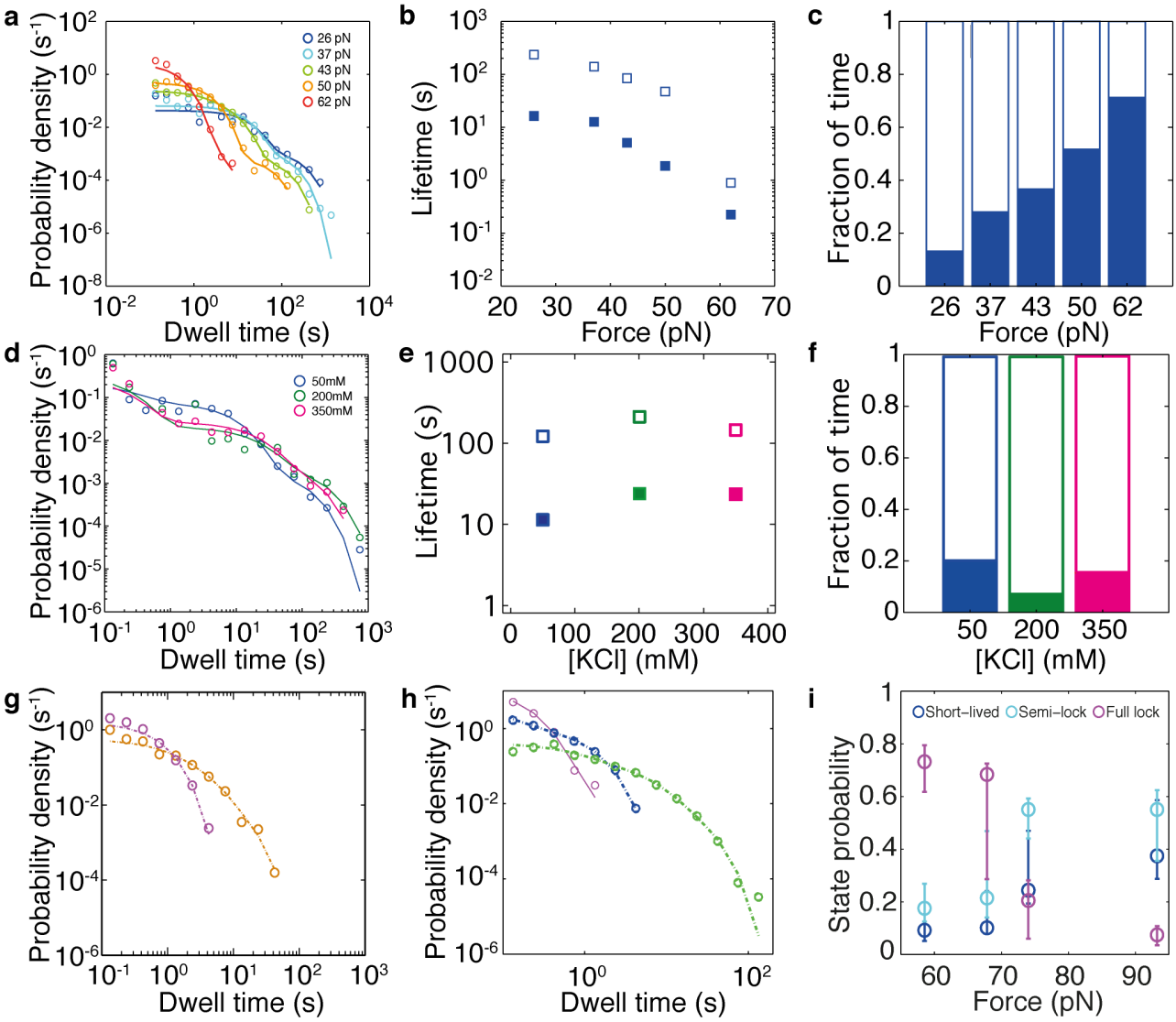

Supplementary Figure 2. Extended characteristics of Tus–*Ter* force-dependent lifetimes. Distribution of lock lifetimes with varying force (**a–c**) or KCl concentration (**d–f**, see text below). The force-dependency was acquired with H144A Tus–*TerB* at 50 mM KCl, and the salt-dependency was acquired with wt Tus–*TerB* at 74 pN. (**a**, **d**) Probability densities (circles) including fits (solid lines). (**b**, **e**) The two longest-lived lifetimes extracted through fitting all datasets (filled squares are the second intermediate state, open squares represent the full lock state). (**c**, **f**) The normalized contribution of each of the fit states to the total experimental time (filled bar is the second state, open bar the full lock state). (**g, h**) Lifetime distributions obtained for the *TerB* GC flipped mutant and permissive orientation. (**g**) Fit probability density distributions of wt Tus and F140A with the GC-flipped *TerB* sequence at 40 pN (purple and orange, respectively). (**h**) Fit probability density distributions of bound-only wt Tus (i.e. in the permissive orientation, purple circles and solid line), H144A combined with the GC flipped *Ter* (blue), and E49K (green) with the GC flipped *Ter* at 19 pN. The lines represent fits to the data. (**i**) Trends in probabilities of all 3 lock states obtained through fitting our 3-state model to the wt Tus–*Ter* dataset.

Nature Chemical Biology: doi:10.1038/nchembio.1857

Salt-dependence of Tus–*Ter* lock

As the reported dissociation constant (K_D) of the Tus–ds*TerB* complex has been shown to be highly salt-dependent, we investigated whether *lock formation* also exhibits a strong salt dependence. We observed that the fraction of rupture events recorded with a lifetime below our cutoff time of 10^{-2} s (i.e., the fraction of open hairpins at t = 0 s) increased from 0% at 50 mM to 14% at 350 mM KCl, while during these experiments care was taken to keep [Tus] well above (at least an order of magnitude) the reported salt-dependent K_D, thereby ensuring the continuous binding of Tus to *Ter*. Concomitantly, we observed that the lifetimes of the two longest-lived exponentials for wt Tus remain virtually unaffected when increasing the [KCl] from 50 to 350 mM, indicating that the lock *strength* is hardly affected by salt concentration (**Supplementary Fig. 2d–f**). In contrast, the reported K_D of the Tus–ds*TerB* complex increases from ~10^{-13} to ~10^{-8} M within the 50 to 350 mM range. We conclude from this that the rate of lock formation is slightly affected by ionic screening, but once the lock is formed its strength remains unaffected. This is in accord with SPR data.

Nature Chemical Biology: doi:10.1038/nchembio.1857

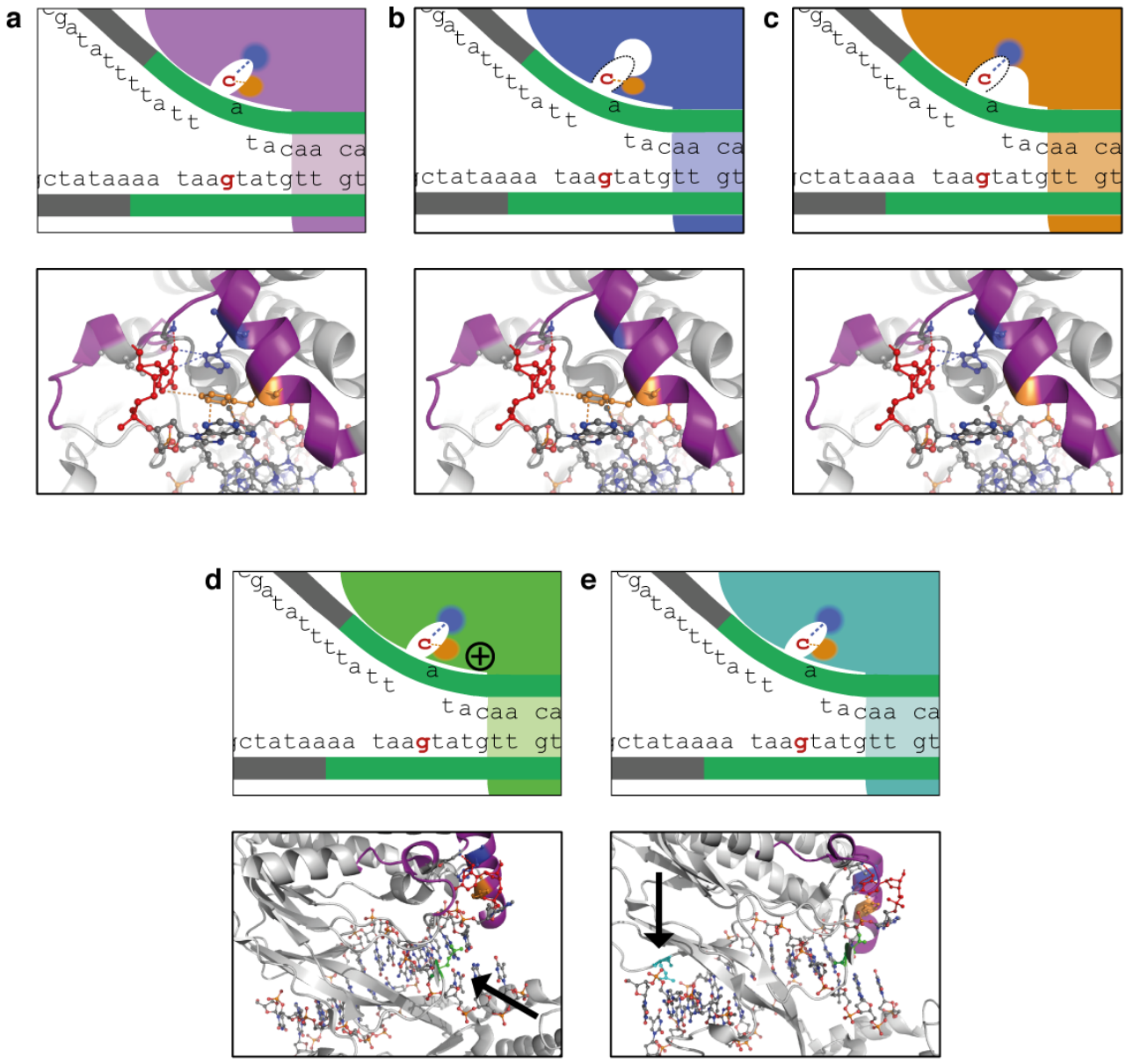

Supplementary Figure 3. Schematic representations of Tus mutations and the corresponding domains in the crystal structure. Shown is the schematic representation of the lock domain of wt Tus (**a**, purple), inner lock domain mutant H144A (**b**, blue), edge lock domain mutant F140A (**c**, orange), outside lock domain mutant E49K (**d**, green) and binding domain mutant Q250A (**e**, cyan), as well as the relevant areas of the crystal structure directly below. Shown is how the C6 base (red) interacts with various amino acids of the lock domain (purple cartoon representation). Since amino acids E49 and Q250 are not part of the lock pocket both amino acids are indicated with an arrow.

Nature Chemical Biology: doi:10.1038/nchembio.1857

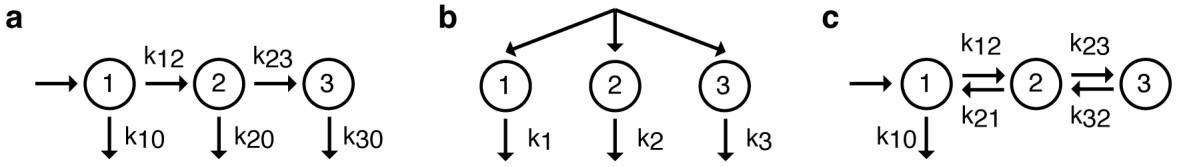

Supplementary Figure 4. Kinetic models that could fit the lifetime distributions. Although there are many different three-state models that can fit our data, we have good reason to assume that our sequential model (**a**) is the simplest that can explain it. We consider it more likely that these substructures are on-pathway intermediate states towards a fully locked state instead of three completely independent structures induced by our pulling experiments, as explained in the Discussion section of the main manuscript. By extracting the rates we find that only the exit rates show a dependence on force (**Main Text Fig. 4b,c**). Interestingly, the inter-state rates (k_{12} and k_{23}) are shielded from the force we subject the Tus–*Ter* system to in our assay. The fact that we observe an exponential dependency on force of only the off-rates implies that the force dependency of the probabilities (supplementary eqns. 4–7) and lifetimes we observe only depend on the state exit rates. **Table 2** contains all the rates of the datasets presented in this work. Depending on the outcome of the Bayes-Schwartz information criterion, either a two or three exponential fit was used. (**b**) If sequential, progressive strengthening of states were not the case, a model with 3 independent states can also fit the data, yielding probabilities (the A's in **Table 1**) very similar to those obtained by fitting our sequential model (P's in **Table 2**). However, now all the parameters of this model display force-dependent trends, as we show that both the state lifetimes as well as the rates underlying the probabilities are force-dependent (**Fig. 2a–c** and **Main Text Fig. 3d**, respectively). (**c**) While there are many more three-state models that can fit our data, all add an additional complexity that cannot be verified by our experiments. This also holds true in the case of the reverse-exit model shown here. But since we are applying large forces to the system, we might modify the exit pathway out of the Tus–*Ter* lock state. While *in vivo* there might be a reverse order of exiting, our high pulling forces likely deform the energy landscape in such a way that other exit pathways also become available. Intuitively this makes sense since reverse exit implies a return of the *Ter* bases at the fork to their base-paired conformation – the forces applied in our experiments will always prevent this from happening.

Nature Chemical Biology: doi:10.1038/nchembio.1857

Supplementary Table 1. The fit parameters to generate the fits (k1–3 and A1-3, equation (1)) as well as the lifetimes associated with each state (τ1-3; the inverse of the respective *k*s). Lower and upper 1-σ CIs are shown left and right below each value respectively.

Dataset	k1 (1/s)	k2 (1/s)	k3 (1/s)	A1	A2	A3	τ1 (s)	τ2 (s)	τ3 (s)
E49K 50mM 59 pN	1.3974	0.2432	0.0011	0.4254	0.5055	0.0691	0.72	4.11	932.63
	1.0512 1.8991	0.2062 0.2793	0.0009 0.0013	0.3463 0.5354	0.3969 0.5865	0.0521 0.0831	0.53 0.95	3.58 4.85	772.62 1097.00
E49KGCf 50mM 19 pN	1.3655	0.2237	0.0646	0.1912	0.5535	0.2554	0.73	4.47	15.47
	0.7784 2.0261	0.1411 0.3062	0.0430 0.0774	0.1253 0.3331	0.4822 0.6200	0.0898 0.3741	0.49 1.28	3.27 7.09	12.92 23.24
E49KGCf 50mM 24 pN	1.7844	0.4405	0.0519	0.9070	0.0748	0.0182	0.56	2.27	19.26
	1.7052 2.0610	0.3415 1.5680	0.0368 0.0919	0.0007 0.9301	0.0543 0.9410	0.0103 0.0348	0.49 0.59	0.64 2.93	10.88 27.16
F140A 50mM 47 pN	7.3335	0.0731	0.0086	0.3966	0.2549	0.3486	0.14	13.68	116.29
	5.9305 12.7417	0.0404 0.3144	0.0060 0.0116	0.3340 0.5092	0.1442 0.3839	0.1902 0.4282	0.08 0.17	3.18 24.75	85.93 167.64
F140A 50mM 50 pN	1.6428	0.0536	0.0097	0.2275	0.5843	0.1882	0.61	18.67	103.08
	1.2645 73.4507	0.0457 0.1169	0.0072 0.0183	0.1837 0.9808	0.0085 0.6500	0.0096 0.2821	0.01 0.79	8.55 21.89	54.65 139.58
F140A 50mM 54 pN	19.6676	0.1630	0.0298	0.3799	0.5430	0.0771	0.05	6.13	33.61
	9.8855 31.1323	0.1476 0.1933	0.0214 0.0463	0.2361 0.6245	0.3010 0.6643	0.0391 0.1347	0.03 0.10	5.17 6.77	21.61 46.62
F140A 50mM 59 pN	4.7211	0.3507	0.0181	0.3139	0.6671	0.0190	0.21	2.85	55.27
	3.4487 6.6327	0.3168 0.3873	0.0153 0.0216	0.2766 0.3735	0.6058 0.7035	0.0107 0.0287	0.15 0.29	2.58 3.16	46.34 65.34
F140AGCf 50mM 35 pN	0.5269	0.0799		0.5382	0.4618		1.90	12.52	
	0.3206 0.9963	0.0509 0.1070		0.3576 0.7469	0.2526 0.6421		1.00 3.12	9.35 19.63	
F140AGCf 50mM 40 pN	1.0714	0.1757		0.5317	0.4683		0.93	5.69	
	0.7378 2.8859	0.1340 0.2331		0.3418 0.6837	0.3163 0.6575		0.35 1.36	4.29 7.46	
F140AGCf 50mM 47 pN	6.1670	0.8115		0.2588	0.7412		0.16	1.23	
	5.1176 7.3741	0.7731 0.8504		0.2269 0.2986	0.7011 0.7725		0.14 0.20	1.18 1.29	
H144A 50mM 24 pN	14.9928	0.0579	0.0042	0.1094	0.6081	0.2825	0.07	17.29	238.43
	0.4369 100.0000	0.0428 0.0691	0.0034 0.0054	0.0725 0.9981	0.0013 0.6432	0.0005 0.3258	0.01 2.29	14.46 23.36	184.54 290.91
H144A 50mM 35 pN	100.0000	0.0779	0.0071	0.9952	0.0039	0.0009	0.01	12.84	141.63
	0.0897 100.0000	0.0137 0.0802	0.0020 0.0092	0.0778 0.9927	0.0057 0.7413	0.0016 0.1938	0.01 11.15	12.47 72.77	108.65 488.25
H144A 50mM 40 pN	0.9332	0.1513	0.0101	0.2001	0.7238	0.0761	1.07	6.61	98.74
	0.6735 14.1291	0.1363 0.1832	0.0087 0.0126	0.1235 0.3013	0.6263 0.7954	0.0572 0.0915	0.07 1.48	5.46 7.34	79.21 114.57
H144A 50mM 47 pN	99.0198	0.5380	0.0211	1.22E-04	0.9645	0.0354	0.01	1.86	47.42
	0.5996 100.0000	0.3750 0.5335	0.0164 0.0255	0.0009 0.9416	0.0481 0.9587	0.0195 0.0418	0.01 1.67	1.87 2.67	39.23 60.86
H144A 50mM 59 pN	6.0193	2.3191	0.4642	0.6550	0.3352	0.0098	0.17	0.43	2.15
	5.3403 99.7892	1.9081 4.5799	0.3036 1.6819	0.0009 0.7652	0.2067 0.7556	0.0037 0.1306	0.01 0.19	0.22 0.52	0.59 3.29
H144AGCf 50mM 19 pN	10.8718	1.2214		0.2124	0.7876		0.09	0.82	
	6.0554 31.3382	1.1389 1.2910		0.1901 0.5849	0.4051 0.8098		0.03 0.17	0.77 0.88	
Q250A 200mM 59pN	50.9000	0.0925	0.0046	0.8098	0.1540	0.0362	0.02	10.81	219.54
	4.5013 67.2385	0.0780 0.1032	0.0038 0.0057	0.4415 0.9364	0.0266 0.4545	0.0042 0.1344	0.01 0.22	9.69 12.82	176.19 262.00
Q250A 50mM 59 pN	7.6697	0.0657	0.0043	0.0928	0.3399	0.5673	0.13	15.23	232.29
	0.2996 10.6434	0.0302 0.1375	0.0035 0.0051	0.0720 0.2221	0.2205 0.4223	0.4427 0.6560	0.09 3.34	7.27 33.13	194.67 286.12
Q250A 50mM 93 pN	100.0000	0.7251	0.0530	0.9980	0.0016	0.0004	0.01	1.38	18.85
	0.9019 100.0000	0.1305 0.7635	0.0196 0.0675	0.3342 0.9985	0.0012 0.5328	0.0003 0.1073	0.01 1.11	1.31 7.67	14.82 50.97
WT 200mM 74 pN	13.7971	0.0486	0.0048	0.2245	0.3365	0.4390	0.07	20.56	206.86
	0.7918 25.0195	0.0252 0.2076	0.0036 0.0066	0.1212 0.4298	0.1575 0.4679	0.2483 0.5759	0.04 1.26	4.82 39.69	151.47 279.95
WT 200mM 93 pN	1.0919	0.1625	0.0311	0.4163	0.5291	0.0547	0.92	6.16	32.19
	0.9192 1.7879	0.1472 0.6839	0.0224 0.0957	0.2012 0.4782	0.4341 0.6032	0.0311 0.3634	0.56 1.09	1.46 6.79	10.45 44.71
WT 350mM 74 pN	12.6376	0.0469	0.0071	0.1848	0.4464	0.3687	0.08	21.31	140.11
	8.8062 17.8469	0.0395 0.0576	0.0063 0.0082	0.1076 0.3063	0.3402 0.5134	0.2751 0.4523	0.06 0.11	17.35 25.32	122.26 157.79
WT-mmTer 50mM 59 pN	0.3550	0.0247	0.0018	0.0998	0.2101	0.6900	2.82	40.51	541.90
	0.1608 3.3106	0.0098 0.0909	0.0017 0.0021	0.0250 0.1608	0.1529 0.3477	0.5258 0.7925	0.30 6.22	11.00 101.61	481.12 600.87
WT 50mM 59 pN	0.7843	0.0343	0.0014	0.0843	0.1514	0.7643	1.27	29.16	720.22
	0.2804 16.0718	0.0175 0.1149	0.0012 0.0016	0.0454 0.1429	0.1021 0.2301	0.6691 0.8218	0.06 3.57	8.70 57.16	636.56 800.91
WT 50mM 68 pN	1.5233	0.0956	0.0050	0.0874	0.1887	0.7239	0.66	10.46	199.68
	0.4821 7.3087	0.0143 0.2429	0.0040 0.0056	0.0649 0.2198	0.1221 0.3548	0.3953 0.7643	0.14 2.07	4.12 70.08	178.31 250.41
WT 50mM 74 pN	23.7187	0.1055	0.0087	0.3150	0.5152	0.1697	0.04	9.48	114.44
	0.2335 44.2823	0.0495 0.1323	0.0051 0.0129	0.1597 0.7889	0.1345 0.6289	0.0323 0.2382	0.02 4.28	7.56 20.19	77.53 194.85
WT 50mM 93 pN	1.8677	0.2205	0.0185	0.3008	0.6167	0.0825	0.54	4.53	54.00
	0.8525 3.6589	0.1434 0.2883	0.0107 0.0300	0.2281 0.5206	0.4123 0.6732	0.0396 0.1219	0.27 1.17	3.47 6.98	33.30 93.39
WTGCf 50mM 29 pN	0.3818	0.0250		0.9539	0.0461		2.62	40.00	
	0.3598 0.4072	0.0198 0.0332		0.9368 0.9689	0.0310 0.0631		2.46 2.78	30.15 50.53	
WTGCf 50mM 35 pN	1.0263	0.2331		0.9370	0.0630		0.97	4.29	
	0.9606 1.4694	0.1381 0.5954		0.5704 0.9713	0.0286 0.4233		0.68 1.04	1.68 7.24	
WTGCf 50mM 40 pN	3.6937	1.4405		0.4913	0.5087		0.27	0.69	
	3.2017 4.4938	1.2980 1.5661		0.3824 0.6074	0.3924 0.6168		0.22 0.31	0.64 0.77	
WTperm 50mM 19pN	7.1863	1.9324		0.9528	0.0472		0.14	0.52	
	6.8488 100.0000	1.5950 5.4160		0.9176 0.9959	0.0039 0.0823		0.01 0.15	0.18 0.63	

Nature Chemical Biology: doi:10.1038/nchembio.1857

Supplementary Table 2. Overview of extracted kinetic rates and probabilities. The probabilities are calculated from the extracted rates using eqns. 4–7. Lower and upper 1-σ CIs are shown left and right below each value respectively.

Dataset	k10 (1/s)	k12 (1/s)	k20 (1/s)	k23 (1/s)	k30 (1/s)	P(1)	P(2)	P(3)
E49K 50mM 59 pN	0.7175 0.6178 0.8735	0.6799 0.4164 1.0609	0.2088 0.1683 0.2431	0.0344 0.0260 0.0431	0.0011 0.0009 0.0013	0.5134 0.4313 0.6088	0.4178 0.3189 0.5016	0.0687 0.0518 0.0825
E49KGCf 50mM 19 pN	0.4013 0.3370 0.4534	0.9642 0.4289 1.5777	0.1689 0.1259 0.2018	0.0548 0.0145 0.1071	0.0646 0.0430 0.0774	0.2939 0.2210 0.4419	0.5331 0.4632 0.5924	0.1730 0.0594 0.2666
E49KGCf 50mM 24 pN	1.6523 1.5699 1.7387	0.1321 0.0962 0.2959	0.3476 0.2455 0.9245	0.0929 0.0446 0.1390	0.0519 0.0368 0.0919	0.9260 0.8486 0.9445	0.0584 0.0425 0.1294	0.0156 0.0087 0.0311
F140A 50mM 47 pN	2.9297 2.0672 5.9511	4.4037 3.5706 6.4214	0.0357 0.0262 0.0896	0.0374 0.0125 0.2314	0.0086 0.0060 0.0116	0.3995 0.3375 0.5115	0.2933 0.1539 0.4174	0.3072 0.1632 0.3969
F140A 50mM 50 pN	0.4068 0.3102 70.4627	1.2360 0.5425 2.0994	0.0427 0.0369 0.0697	0.0109 0.0063 0.0462	0.0097 0.0072 0.0183	0.2476 0.2049 0.9809	0.5992 0.0083 0.6533	0.1532 0.0085 0.2249
F140A 50mM 54 pN	7.5623 2.3778 19.4368	12.1052 6.9996 12.8166	0.1464 0.1351 0.1633	0.0167 0.0104 0.0330	0.0298 0.0214 0.0463	0.3845 0.2472 0.6264	0.5526 0.3180 0.6683	0.0629 0.0329 0.1050
F140A 50mM 59 pN	1.7161 1.3277 2.3275	3.0050 2.0426 4.3437	0.3408 0.3072 0.3759	0.0099 0.0057 0.0156	0.0181 0.0153 0.0216	0.3635 0.3258 0.4231	0.6185 0.5566 0.6532	0.0180 0.0102 0.0271
F140AGCf 50mM 35 pN	0.3205 0.2516 0.4502	0.2064 0.0661 0.5809	0.0799 0.0509 0.1070			0.6082 0.4230 0.7902	0.3918 0.2094 0.5746	
F140AGCf 50mM 40 pN	0.6519 0.5387 1.1811	0.4195 0.1928 1.7212	0.1757 0.1340 0.2331			0.6085 0.3942 0.7371	0.3915 0.2628 0.6057	
F140AGCf 50mM 47 pN	2.1976 1.8948 2.5662	3.9695 3.1183 4.8638	0.8115 0.7731 0.8504			0.3563 0.3258 0.3966	0.6437 0.6031 0.6741	
H144A 50mM 24 pN	1.6761 0.0597 99.8145	13.3167 0.1211 11.2308	0.0408 0.0284 0.0472	0.0171 0.0101 0.0244	0.0042 0.0034 0.0054	0.1118 0.0948 0.9981	0.6262 0.0014 0.6512	0.2620 0.0005 0.2954
H144A 50mM 35 pN	99.5198 0.0692 98.7552	0.4802 0.0206 3.7824	0.0645 0.0123 0.0654	0.0133 0.0012 0.0164	0.0071 0.0020 0.0092	0.9952 0.1038 0.9927	0.0040 0.0060 0.7292	0.0008 0.0014 0.1699
H144A 50mM 40 pN	0.2970 0.2693 2.1655	0.6362 0.3850 10.4933	0.1357 0.1214 0.1672	0.0156 0.0120 0.0193	0.0101 0.0087 0.0126	0.3183 0.1498 0.4269	0.6115 0.5092 0.7732	0.0702 0.0527 0.0848
H144A 50mM 47 pN	0.5317 0.5321 0.6938	98.4881 0.0348 99.1527	0.5196 0.1296 0.5133	0.0184 0.0133 0.0338	0.0211 0.0164 0.0255	0.0054 0.0066 0.9521	0.9606 0.0454 0.9545	0.0340 0.0144 0.0392
H144A 50mM 59 pN	4.7245 4.2569 5.4003	1.2947 0.7782 93.3624	2.2411 1.7924 3.7682	0.0780 0.0272 0.5556	0.4642 0.3036 1.6819	0.7849 0.0566 0.8541	0.2079 0.1179 0.6938	0.0072 0.0026 0.0699
H144AGCf 50mM 19 pN	3.2712 2.2090 16.4183	7.6006 3.0051 11.3265	1.2214 1.1389 1.2910			0.3009 0.2984 0.6109	0.6991 0.3880 0.7015	
Q250A 200mM 59pN	41.2326 0.1296 62.9968	9.6673 0.2685 15.1011	0.0757 0.0607 0.0850	0.0168 0.0105 0.0227	0.0046 0.0038 0.0057	0.8101 0.4522 0.9365	0.1555 0.0302 0.4397	0.0345 0.0015 0.1114
Q250A 50mM 59 pN	0.7363 0.0685 1.3946	6.9334 0.2295 9.2923	0.0272 0.0120 0.0419	0.0385 0.0158 0.0960	0.0043 0.0035 0.0051	0.0960 0.0754 0.2423	0.3742 0.2475 0.4587	0.5298 0.3921 0.6220
Q250A 50mM 93 pN	99.8000 0.6705 99.8517	0.2000 0.1319 1.8363	0.5982 0.1116 0.6188	0.1269 0.0141 0.1521	0.0530 0.0196 0.0675	0.9980 0.4295 0.9985	0.0016 0.0012 0.4628	0.0003 0.0002 0.0938
WT 200mM 74 pN	3.1162 0.1255 9.2143	10.6808 0.6257 14.0952	0.0238 0.0134 0.0460	0.0248 0.0091 0.1560	0.0048 0.0036 0.0066	0.2259 0.1321 0.4473	0.3789 0.1766 0.5026	0.3952 0.2161 0.5324
WT 200mM 93 pN	0.5422 0.4687 0.6504	0.5497 0.4218 1.0533	0.1486 0.1302 0.1914	0.0139 0.0081 0.2583	0.0311 0.0224 0.0957	0.4965 0.3657 0.5605	0.4605 0.3760 0.5497	0.0429 0.0252 0.2822
WT 350mM 74 pN	2.3591 0.9963 4.6580	10.2785 7.3901 13.0933	0.0289 0.0243 0.0342	0.0180 0.0128 0.0259	0.0071 0.0063 0.0082	0.1867 0.1142 0.3076	0.5009 0.3946 0.5647	0.3125 0.2307 0.3847
WT-mmTer 50mM 59 pN	0.0354 0.0220 0.0819	0.3196 0.1340 3.1424	0.0058 0.0031 0.0149	0.0189 0.0061 0.0759	0.0018 0.0017 0.0021	0.0844 0.0113 0.1427	0.1659 0.1212 0.2675	0.7497 0.6378 0.8222
WT 50mM 59 pN	0.0724 0.0348 0.1660	0.7120 0.2442 14.2307	0.0066 0.0034 0.0147	0.0277 0.0127 0.0925	0.0014 0.0012 0.0016	0.0923 0.0514 0.1529	0.1756 0.1250 0.2689	0.7321 0.6171 0.7943
WT 50mM 68 pN	0.1548 0.0787 0.3782	1.3685 0.3884 6.7703	0.0228 0.0082 0.0454	0.0728 0.0059 0.1986	0.0050 0.0040 0.0056	0.1016 0.0787 0.2401	0.2147 0.1402 0.4683	0.6837 0.2857 0.7249
WT 50mM 74 pN	7.5284 0.1225 31.3348	16.1903 0.1107 15.5270	0.0815 0.0320 0.0958	0.0241 0.0083 0.0388	0.0087 0.0051 0.0129	0.3174 0.1700 0.7980	0.5270 0.1516 0.6338	0.1556 0.0264 0.2113
WT 50mM 93 pN	0.6994 0.4852 1.0736	1.1683 0.3525 2.5548	0.1942 0.1275 0.2459	0.0264 0.0117 0.0462	0.0185 0.0107 0.0300	0.3745 0.2877 0.5864	0.5508 0.3557 0.6237	0.0748 0.0356 0.1077
WTGCf 50mM 29 pN	0.3654 0.3439 0.3888	0.0164 0.0109 0.0228	0.0250 0.0198 0.0332			0.9569 0.9421 0.9711	0.0431 0.0289 0.0579	
WTGCf 50mM 35 pN	0.9763 0.9197 1.1469	0.0500 0.0244 0.3774	0.2331 0.1381 0.5954			0.9513 0.7458 0.9754	0.0487 0.0246 0.2529	
WTGCf 50mM 40 pN	2.5475 2.3883 2.7553	1.1462 0.7434 1.7795	1.4405 1.2980 1.5661			0.6897 0.6008 0.7686	0.3103 0.2313 0.3976	
WTperm 50mM 19pN	6.9384 6.5977 99.5651	0.2479 0.1189 0.4407	1.9324 1.5950 5.4160			0.9655 0.9421 0.9968	0.0345 0.0032 0.0578	

Nature Chemical Biology: doi:10.1038/nchembio.1857

The exponential fit has the general form of:

$$P(t) = \sum_{i=1}^{N} A_i e^{-k_i t} \qquad (1)$$

where *N* is the number of exponentials determined by the BIC. In our kinetic model (**Supplementary Fig. 4a**) the general rates (k_i) and probabilities (A_i) are expressed in terms of the five state associated rates, with

$$\begin{aligned}
k_1 &= k_{10} + k_{12} \\
k_2 &= k_{20} + k_{23} \\
k_3 &= k_{30} \\
A_1 &= \frac{k_{10}^2 + k_{10}k_{12} - k_{10}k_{20} - k_{12}k_{20} - k_{10}k_{23} - k_{10}k_{30} + k_{20}k_{30} + k_{23}k_{30}}{(k_{10} + k_{12} - k_{20} - k_{23})(k_{10} + k_{12} - k_{30})} \\
A_2 &= \frac{k_{12}k_{20} - k_{12}k_{30}}{(k_{10} + k_{12} - k_{20} - k_{23})(k_{20} + k_{23} - k_{30})} \\
A_3 &= \frac{k_{12}k_{23}}{(k_{10} + k_{12} - k_{30})(-k_{20} - k_{23} + k_{30})} \qquad (2)
\end{aligned}$$

for the 3-exponential model, and

$$\begin{aligned}
k_1 &= k_{10} + k_{12} \\
k_2 &= k_{20} \\
A_1 &= \frac{k_{10} - k_{20}}{k_{10} + k_{12} - k_{20}} \\
A_2 &= \frac{k_{12}}{k_{10} + k_{12} - k_{20}} \qquad (3)
\end{aligned}$$

for the 2-exponential model.

$$P(1) = \frac{k_{10}}{k_{10} + k_{12}} \qquad (4)$$

$$P(2) = \frac{k_{12}}{k_{10} + k_{12}} \qquad \text{(2-exp fit)} \qquad (5)$$

$$P(2) = \frac{k_{12}}{k_{10} + k_{12}} \cdot \frac{k_{20}}{k_{20} + k_{23}} \qquad \text{(3-exp fit)} \qquad (6)$$

$$P(3) = \frac{k_{12}}{k_{10} + k_{12}} \cdot \frac{k_{23}}{k_{20} + k_{23}} \qquad (7)$$

Nature Chemical Biology: doi:10.1038/nchembio.1857